COMMUNICATION

Check for updates

Multifunctional carbon dots with near-infrared absorption and emission for targeted delivery of anticancer drugs, tumor tissue imaging and chemo/photothermal synergistic therapy†

Yuefang Hu, [ID] ‡[ab] Liangliang Zhang, [ID] ‡[a] Shengyu Chen,[a] Li Hou,[a] Shulin Zhao, [ID] *[a] Yong Huang[a] and Hong Liang*[a]

Cancer therapy faces considerable challenges related to improving treatment efficiency and overcoming damage to healthy cells. To address these concerns, a strategy for tumor microenvironment-induced cancer imaging/drug release and synergistic chemo–photothermal therapy (chemo/PTT) is proposed in this study. Carbon dots with near-infrared (NIR) absorption and emission, referred to as RCDs, were first prepared and covalently coupled with a Pt(IV) prodrug to form a complex, referred to as RCD–Pt(IV). The surface of the prepared complex was then coated with the polyethylene glycol–chitosan–2,3-dimethylmaleic anhydride polymer (PEG–CS–DA) to obtain a tumor-targeted multifunctional nanoprobe (RCD–Pt(IV)/PEG–CS–DA). When the nanoprobe RCD–Pt(IV)/PEG–CS–DA entered the tumor cells, the acidic environment of the tumor cells allowed rapid PEG–CS–DA hydrolysis and RCD–Pt(IV) release. High levels of glutathione (GSH) in cancer cells reduced Pt(IV) to Pt(II) and released the RCDs, resulting in cancer tissue imaging and targeted Pt(II) release. Meanwhile, Pt(II) collected in the tumor tissues could realize targeted chemotherapy, and the RCDs in the tumor tissues absorbed light energy under NIR light irradiation to produce a large amount of heat to quickly eliminate cancer cells. Thus, cancer tissue imaging/targeted drug release and synergistic chemo/PTT were achieved simultaneously.

Introduction

The combination of imaging diagnosis and targeted therapy can provide personalized precision treatment for cancer patients.[1,2]

Despite significant progress in cancer diagnosis and treatment in recent decades, cancer is still one of the main causes of death in humans. Patients treated with conventional chemotherapy *in vivo* typically experience serious side effects, including the inhibition of hematopoietic function, gastrointestinal toxicity, and cardiac toxicity.[3,4] Photothermal therapy (PTT) provides a new model for cancer treatment. It can convert light energy, particularly near-infrared (NIR) light, into heat energy by using a photothermal agent. In PTT, the temperature of tumor tissue exceeds 50 °C, and the tumor cells are killed quickly.[5,6] Owing to the desirable photothermal properties of nanomaterials, their application as agents for PTT of tumors has drawn wide research interest in biomedicine. NIR light is an electromagnetic wave between visible and mid-infrared light with deep penetration, low water absorption, high spatial and temporal resolution characteristic. Therefore, PTT has become a safe, efficient, noninvasive, and fixed-point treatment with almost no side effects.[7–9] However, the uneven heat distribution of photothermal agents during laser irradiation impedes the complete inhibition of tumor growth when solely PTT is used.[10] To enhance the effectiveness of tumor therapy, a synergistic therapy has been developed, which combines chemotherapy,[11] radiotherapy,[12] photodynamic therapy,[13] and gene therapy or immunotherapy[14] with PTT.[15] This approach considerably improves the efficiency of treatment. High fever due to PTT can enhance cell uptake and release of chemotherapeutic drugs, inhibit tumor resistance to various drugs, and enhance the efficiency of chemotherapy.[16] Meanwhile, chemotherapy is a continuous treatment without space restriction, which can compensate for the deficiency of PTT. Therefore, chemo–photothermal synergistic therapy (chemo/PTT) is recognized as one of the most effective techniques.

Cisplatin or Pt(II), an efficient antitumor drug, has been widely used in the treatment of various solid tumors, such as bladder cancer, testicular cancer, and ovarian cancer.[17] However, Pt(II) lacks tumor specificity, and its severe toxic side effects and intrinsic tumor resistance present serious problems in clinical practice.[18] To reduce the side effects of Pt(II), cisplatin

[a]State Key Laboratory for the Chemistry and Molecular Engineering of Medicinal Resources, School of Chemistry and Pharmaceutical Sciences, Guangxi Normal University, Guilin 541004, China. E-mail: zhaoshulin001@163.com; hliang@gxnu.edu.cn

[b]College of Materials and Environmental Engineering, Hezhou University, Hezhou 542899, China
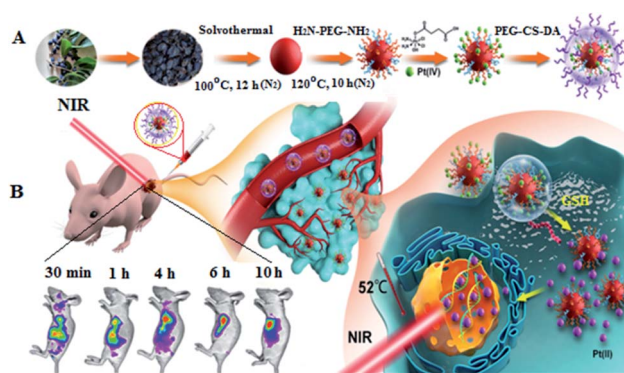
‡ These authors contributed equally to this work and should be considered cofirst authors.

derivatives have been used for tumor therapy. These derivatives include lobar platinum and oxaliplatin, among others. One disadvantage of using cisplatin derivatives for tumor treatment is its potential to reduce drug load or antitumor activity.[19,20] Meanwhile, the Pt(IV) prodrug has also been used in tumor therapy because of its insignificant toxic side effects and the inclusion of two derived functional groups that are easy to covalently modify.[21,22] When Pt(IV) enters cancer cells, the reducing environment within cancer cells reduces Pt(IV) to Pt(II), releasing active units and axial ligands. Pt(II) binds to DNA and causes DNA damage, and axial ligands exhibit biological activity and interact with Pt(II) to kill cancer cells.

Imaging-guided drug delivery and therapy provides a noninvasive alternative approach to surgical resection and systemic drug delivery, which allows high concentrations of drugs to accumulate at tumor sites, reducing both the toxic side effects of drugs on normal cells and tissues and drug loss. The drug can be transported to the tumor site for release, achieving efficient targeted tumor therapy. Although imaging-guided drug delivery is an ideal approach for cancer therapy, its clinical applications remain limited because of the potential toxicity and rapid clearance of currently available imaging agents. Currently, drugs are adsorbed on the surface of nanoparticles by simple physical adsorption in most drug transport systems. After the drugs are carried into organisms, the drug molecules adsorbed on the surface of nanoparticles are released from the surface of nanoparticles into the blood. That is, some drug molecules enter the blood or remain in the surrounding tissue of the tumor site before reaching the tumor site itself, preventing effective drug aggregation at the tumor site and affecting the therapeutic efficacy. The pH value of the normal physiological environment in the human body is about 7.4, and that of the tumor cell microenvironment ranges from 6.5 to 6.8. Thus, the development of a nanocarrier system for drug release induced by the tumor microenvironment, and the realization of active targeted drug transport and release to tumor cells can not only reduce the toxic side effects on normal cells but also considerably improve the therapeutic effect of cancer treatment.

Carbon dots (CDs) are carbon-based nanomaterials with fluorescent properties. The use of CDs has gained research interest because of their distinct chemical properties, such as long fluorescence lifetime, good photostability, low cytotoxicity, and good biocompatibility.[23] CDs have been used as photothermal reagents for PTT.[24,25] Moreover, CDs have been used as nanocarriers for imaging-guided drug transport and chemotherapy because of their superior water solubility and sensitive fluorescence emission properties.[26] However, most of the currently developed CDs can only emit fluorescence in the visible region, which limits their imaging applications *in vivo*.

To address the aforementioned problems, we proposed a strategy for efficient cancer therapy: *in vivo* fluorescence imaging-guided drug delivery/tumor microenvironment-induced release and synergistic chemo/PTT targeted therapy. We first prepared CDs with NIR absorption and emission, referred to as RCDs, and covalently coupled them with the Pt(IV) prodrug to form a positively charged complex: RCD–Pt(IV). The

Scheme 1 Schematic of the preparation of the RCD–Pt(IV)/PEG–CS–DA nanocomposite (A) and the mechanism enabling tumor microenvironment-induced fluorescence imaging/drug release and chemo/PTT synergistic targeted therapy (B).

negatively charged polyethylene glycol–chitosan–2,3-dimethyl maleic anhydride polymer (PEG–CS–DA) was subsequently coated on its surface by charge attraction, forming the multifunctional nanoprobe with a negatively charged surface: RCD–Pt(IV)/PEG–CS–DA (Scheme 1A). This kind of nanoprobe with a negatively charged surface cannot adsorb biological macromolecules, proteins, and normal cell membranes during *in vivo* transmission.[27,28] After the probe was injected into the tail vein of the mouse, NIR luminescence features can be used for cancer imaging *in vivo* to guide the transport of antitumor drugs. When RCD–Pt(IV)/PEG–CS–DA was actively enriched to slightly acidic tumor sites *via* its hyperosmotic long retention effect (EPR) on tumor cells, PEG–CS–DA exhibited a positive charge flip in an acidic tumor, leading to RCD–Pt(IV) release. Meanwhile, high levels of glutathione (GSH) in cancer cells reduced Pt(IV) to highly toxic Pt(II) and released the RCDs. Pt(II) that accumulated in tumor tissue could achieve targeted chemotherapy, whereas the RCDs accumulated in tumor tissue could not only provide an image of the cancer tissue, but also could absorb NIR light to produce a large amount of heat, which can quickly kill cancer cells, achieving imaging-guided chemo/PTT synergistic targeted therapy (Scheme 1B).

Results and discussion

Osmanthus seeds, which are rich in chlorophyll and the elements C, N, and O, can be prepared as CDs by using an appropriate method. In this study, the skin of *Osmanthus* seeds was used as the raw material. CDs with NIR absorption and emission characteristics (RCDs) were prepared using the solvothermal method under nitrogen protection. The morphology and particle size of the RCDs were characterized by transmission electron microscopy (TEM). The results are presented in Fig. 1A and B. As shown in the figure, the RCDs exhibit good dispersibility, with diameters of about 1.0–3.5 nm, and an average particle size of 2.2 nm. High-resolution TEM (HTEM) imaging showed a lattice spacing of 0.32 nm, corresponding to the lattice spacing of graphite diffraction (002). RCD composition and surface bonding were characterized by X-ray
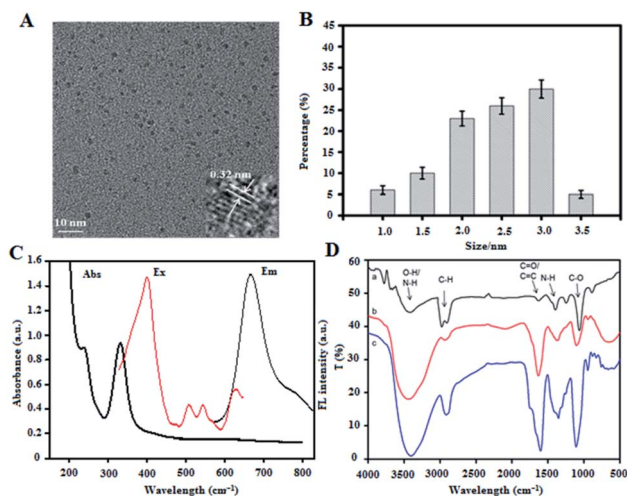
Fig. 1 (A) TEM image of the RCDs. (B) Diameter distribution of RCDs. (C) UV-vis absorption and fluorescence excitation and emission spectra of RCDs. (D) FTIR spectra of RCDs (curve a), RCD–Pt(IV) (curve b), and RCD–Pt(IV)/PEG–CS–DA (curve c).

photoelectron spectroscopy (XPS), and the results are shown in Fig. S1a (ESI†). The diagram shows three typical peaks at 284.9, 398.9, and 531.9 eV in the XPS full-scan spectrum, corresponding to C 1s, N 1s, and O 1s, respectively. These observations indicate that the RCDs mainly consist of the elements C, N, and O with relative percentages of 65.31%, 4.04%, and 30.07%, respectively. The high-resolution spectra of C 1s also show three peaks at 284.4, 285.8, and 287.9 eV (Fig. S1b, ESI†), indicating the presence of the C–C/C=C, C–N/C–O, and C=N/C=O bonds on the RCD surface. The high-resolution spectra of N 1s have two peaks at 399.4 and 400.5 eV (Fig. S1c, ESI†), corresponding to N–H and C–N/N–N, respectively—that is, pyridine nitrogen and pyrrole nitrogen. The high-resolution spectra of O1s have two peaks at 531.2 and 532.5 eV (Fig. S1d, ESI†), corresponding to the C=O and C–O bonds, respectively. To evaluate the optical properties of the RCDs, their fluorescence and UV-vis spectra were recorded. Fig. 1C shows the UV-vis absorption spectrum and fluorescence excitation and emission spectra of the RCDs at room temperature. In the figure, the UV-vis absorption spectrum shows a wide absorption band from 200 nm to 800 nm, indicating that the RCDs still exhibit strong absorption in the NIR region from 650 nm to 800 nm, and the photothermal conversion efficiency was calculated to be 34%. This feature renders the RCDs suitable for PTT. Moreover, the maximum fluorescence emission wavelength of the RCD solution is 680 nm under light excitation of 417 nm. As shown in the excitation spectrum, except for the maximum excitation peak at 417 nm, several small fluorescence excitation peaks at 512, 544, and 630 nm are observed in the RCD solution. These results indicate that the prepared RCDs exhibit NIR absorption and emission characteristics, which provides a basis for their application in *in vivo* imaging and PTT of tumors.

RCDs, Pt(IV) prodrugs (c,c,t-[PtCl$_2$(OH)(NH$_3$)$_2$(O$_2$CCH$_2$CH$_2$CO$_2$H)]) and PEG–CS–DA were prepared. The RCDs were then covalently coupled with the Pt(IV) prodrug to obtain RCQD–

Pt(IV). Finally, PEG–CS–DA with a negative charge and RCQD–Pt(IV) with a positive charge form RCD–Pt(IV)/PEG–CS–DA by electrostatic attraction. The RCDs, RCD–Pt(IV), and RCD–Pt(IV)/PEG–CS–DA were characterized by Fourier transform infrared spectroscopy (FTIR). The results are presented in Fig. 1D. In the FTIR spectrum of the RCDs (curve a), the peak at 1055 cm^{-1} belongs to the bending vibration of the C–O bond, showing major absorption bands associated with carboxyl groups; the peak at 1380 cm^{-1} is ascribed to the stretching vibration of the N–H bond; and the peak at 1640 cm^{-1} is attributed to the C=O stretching vibration. The absorption band at 3443 cm^{-1} is assigned to the O–H and N–H bonds, indicating the presence of many amino and carboxyl groups on the surface of the RCDs, improving the hydrophilicity, stability, and modifiability of RCDs. Curve b represents the FTIR spectrum of RCD–Pt(IV). The vibration intensity of the C=O and N–H bonds in the spectral curve increases relative to that of RCDs, indicating that the Pt(IV) prodrug has been successfully modified into the RCDs. The FTIR spectrum of RCD–Pt(IV)/PEG–CS–DA is also shown in Fig. 1D (curve c). Compared with the FTIR spectrum of RCD–Pt(IV), the peak strength of various functional groups is significantly enhanced, indicating the successful combination of RCD–Pt(IV) and PEG–CS–DA. The zeta potentials of the RCDs and RCD–Pt(IV) were also measured. The results in Fig. S2 (ESI†) show that the RCDs have a zeta potential of 18.0 mV; the positive charge is attributed to the existence of a large number of amino groups on the surface. The RCDs loaded with Pt(IV) have a zeta potential of 10.7 mV. The decrease in zeta potential is attributed to the binding of the Pt(IV) prodrug to the RCDs. Some positively charged amino groups on the RCDs are
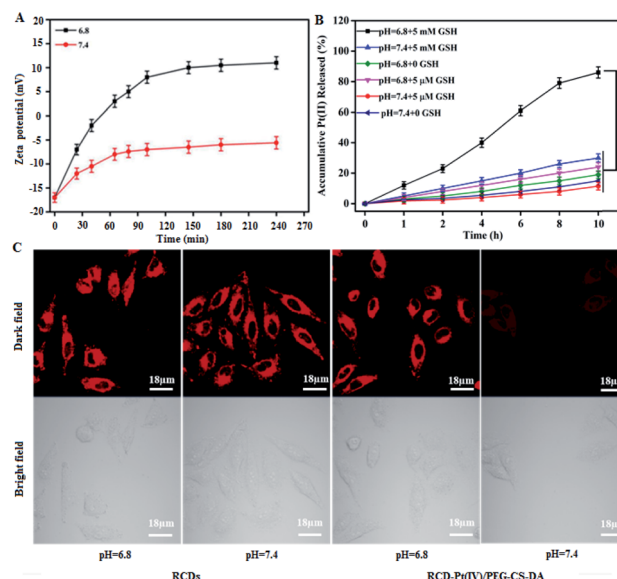

Fig. 2 (A) Zeta potential of RCD–Pt(IV)/PEG–CS–DA under different conditions. (B) The effect of pH value and GSH concentration in the medium on the RCD–Pt(IV)/PEG–CS–DA releasing Pt (II). (C) Laser confocal fluorescence imaging of T24 cells after incubation (excitation: 405 nm; emission: 680 nm). The error bar represents the standard deviation ($n = 3$). The statistical analysis was performed using the Student's t-test method, ***$p < 0.001$.

covalently coupled to the carboxyl groups on the Pt(IV) prodrug. Consequently, the zeta potential of RCD–Pt(IV) is lower than that of the RCDs. The resulting zeta potential measurements further indicate the successful coupling of the Pt(IV) prodrug to the RCDs. The UV-vis absorption spectrum of RCD–Pt(IV) is similar to that of the RCDs (Fig. S3, ESI†), indicating that the combination of the Pt(IV) prodrug with the RCDs does not affect the UV absorption properties of the RCDs; moreover, it shows strong absorption in the NIR region, which is suitable as a photothermal reagent for PTT.

To determine whether the tumor microenvironment can induce targeted release of antitumor drugs, the change of the zeta potential for the probe (RCD–Pt(IV)/PEG–CS–DA) was examined under normal physiological (pH 7.4) and the tumor cell microenvironment (pH 6.8) conditions. The probe was incubated with a phosphate buffer solution (pH 6.8 and 7.4) at 37 °C. The zeta potential of the probe at different incubation times in both solutions was then measured. The results indicated that at pH 6.8, the zeta potential of RCD–Pt(IV)/PEG–CS–DA increased from −17 mV to 10.9 mV as the incubation time was extended, showing a charge flip from negative to positive. At pH 7.4, RCD–Pt(IV)/PEG–CS–DA still exhibited charge non-flipping properties after incubation for 4 h and a more constant negative charge (Fig. 2A). Subsequently, the ability of RCD–Pt(IV)/PEG–CS–DA releasing Pt(II) at different concentrations of GSH was evaluated at varying pH values. RCD–Pt(IV)/PEG–CS–DA (15 mg) was added to the PBS solution containing different concentrations of GSH at varying pH values, and then dialyzed in ultrapure water for 10 h at 37 °C. Pt in the dialysate was subsequently detected by inductively-coupled plasma mass spectrometry (ICP-MS) analysis. The drug release curve of Pt(II) within 10 h is presented in Fig. 2B. In the diagram, the concentration of GSH and the pH value of the PBS solution obviously influence the release rate of Pt(II). When the concentration of GSH was close to that of normal extracellular plasma (5 μM), only about 20% of Pt(II) was released at pH 6.8, and a lower release rate at pH 7.4 after 6 h of dialysis was observed. When the concentration of GSH was close to that of cancer cells (5 mM), the release rate of Pt(II) significantly increased. After 6 h of dialysis, 61% of Pt(II) was released at pH 6.8. After 10 h of dialysis, the release rate of Pt(II) exceeded 85%. At pH 7.4, when the GSH concentrations were 5 μM and 5 mM, the release rate of Pt(II) was less than 20%. These results confirm that RCD–Pt(IV)/PEG–CS–DA can release Pt(II) in large quantities only in a slightly acidic (pH 6.8) and high-concentration GSH environment. To further demonstrate the reliability of the aforementioned conclusions, cancer cells (T24 cells) were incubated with RCDs and RCD–Pt(IV)/PEG–CS–DA for 4 h at pH 6.8 and 7.4 at 37 °C. Subsequently, fluorescence imaging of T24 cells was performed by laser confocal fluorescence microscopy (CLSM), and the results are presented in Fig. 2C. At pH = 6.8 and 7.4, the two groups of T24 cells incubated with RCDs all exhibited strong red fluorescence. However the two groups of T24 cells incubated with RCD–Pt(IV)/PEG–CS–DA showed strong red fluorescence only at pH 6.8. The reason is that red fluorescence could be emitted at both pH = 6.8 and pH = 7.4 after the free RCDs entered the cell. After RCD–Pt(IV)/PEG–CS–DA entered the

cell, PEG–CS–DA could only be hydrolyzed into a positively charged complex at pH = 6.8; meanwhile, positively charged RCD–Pt(IV) was released by electrostatic repulsion. The intracellular GSH reduced Pt(IV) to Pt(II) and removed two axially derived groups, simultaneously releasing RCDs, producing red fluorescence emission. This behavior of RCD–Pt(IV)/PEG–CS–DA toward the GSH concentration and pH value dependence and sensitivity effectively prevented the loss of Pt(II) during blood circulation, and targeted Pt(II) release to the tumor site. It not only enhanced the efficacy of tumor therapy but also reduced its toxicity in the whole body.

The increase in ambient temperature in tumor tissue increases the permeability of the peripheral vascular wall and tumor cell membrane, facilitating the entry of antitumor drugs into tumor cells. Thus, in PTT, photothermal effects of RCDs increase the cytotoxicity of Pt(II).[29,30] Thus, the efficacy of RCD–Pt(IV)/PEG–CS–DA for chemo/PTT synergistic therapy of cancer cells was evaluated. A549 cells were incubated with different concentrations of RCDs and RCD–Pt(IV)/PEG–CS–DA for 24 h. The survival rate of cells in different experimental groups was determined directly; alternatively, the survival rate of cells in different experimental groups was evaluated after irradiation with a 680 nm laser (1.5 W cm^{-2}) for 3 min. The results are presented in Fig. 3A. As observed in the diagram, the concentration of RCDs or RCD–Pt(IV)/PEG–CS–DA in the cell incubation medium ranges from 0.1 μM to 100 μM. The toxicity of RCDs to A549 cells was negligible, and the cell survival rate was about 90%. Meanwhile, the toxicity of RCD–Pt(IV)/PEG–CS–DA to A549
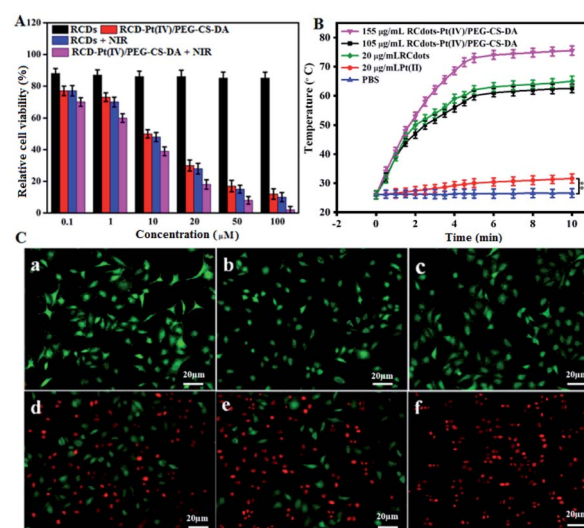

Fig. 3 (A) Cell survival of T24 cells after incubation for 24 h with RCDs and RCD–Pt(IV)/PEG–CS–DA under different conditions. (B) Temperature change of PBS, Pt(II), RCD, and RCD–Pt(IV)/PEG–CS–DA solutions at different irradiation times. (C) CLSM fluorescence images of live and dead T24 cells stained with calcein–AM and propidium iodide. (a) PBS; (b) PBS + NIR laser irradiation; (c) 20 mg mL^{-1} RCDs; (d) 20 mg mL^{-1} RCDs + NIR laser irradiation; (e) 105 mg mL^{-1} RCD–Pt(IV)/PEG–CS–DA; (f) 105 mg mL^{-1} RCD–Pt(IV)/PEG–CS–DA + NIR laser irradiation. The error bar represents the standard deviation ($n = 3$). The statistical analysis was performed using the Student's t-test method, **$p < 0.01$.

cells gradually increased with increasing concentration, and the cell survival rate decreased from 90% to about 13%, indicating that RCD–Pt(ɪᴠ)/PEG–CS–DA with a satisfactory chemotherapeutic effect could kill A549 cells. After irradiation with a 680 nm laser (1.5 W cm^{-2}) for 3 min, the cell survival in the RCD group decreased from 90% to about 10%, suggesting that RCDs could produce a large amount of heat to kill A549 cells, and exerted a satisfactory PTT effect. The cell survival rate in the RCD–Pt(ɪᴠ)/PEG–CS–DA group decreased from 90% to less than 2%, and the cancer cells were killed almost completely, indicating that the RCD–Pt(ɪᴠ)/PEG–CS–DA exerted a good chemo and photodynamic synergistic therapeutic effect. To optimize the PTT conditions, the effects of illumination time on the photothermal efficiency were evaluated under different conditions. The results are presented in Fig. 3B. As can be seen in the diagram, no change in the temperature was observed in the PBS and Pt(ɪɪ) groups under laser illumination over a period of 10 min, indicating that the PBS and Pt(ɪɪ) solutions could not exert photothermal effects. However, the temperature of the 20 μg mL^{-1} RCD and 105 μg mL^{-1} RCD–Pt(ɪᴠ)/PEG–CS–DA (load = 20 μg mL^{-1} RCDs) groups could reach about 60 °C under laser irradiation over a period of 5 min. No significant difference in photothermal effects was observed between the 20 μg mL^{-1} RCD solution and the 105 μg mL^{-1} RCD–Pt(ɪᴠ)/PEG–CS–DA solution (load equal RCDs), indicating that the capabilities of RCD–Pt(ɪᴠ)/PEG–CS–DA and RCDs for photothermal conversion were similar. Moreover, when the concentration of the RCD–Pt(ɪᴠ)/PEG–CS–DA solution was increased to 155 μg mL^{-1}, the photothermal effect increased significantly, indicating that the photothermal effect of the RCD–Pt(ɪᴠ)/PEG–CS–DA solution was significantly concentration-dependent. The aforementioned experimental results also proved that the RCDs modified with Pt(ɪᴠ) and PEG–CS–DA failed to reduce the photothermal effect of RCDs. Therefore, RCD–Pt(ɪᴠ)/PEG–CS–DA can be used as an ideal chemo/PTT agent for efficient tumor treatment.

For a more intuitive observation of the synergistic therapeutic effect of RCD–Pt(ɪᴠ)/PEG–CS–DA on tumor cells, the photothermal toxicity of the drug loading system to cancer cells was examined by cell staining. The cultured T24 cells were divided into six groups, including PBS, PBS + NIR laser irradiation, RCDs, RCDs + NIR laser irradiation, RCD–Pt(ɪᴠ)/PEG–CS–DA, and RCD–Pt(ɪᴠ)/PEG–CS–DA + NIR laser irradiation. The cells were then stained and subjected to CLSM. The results are presented in Fig. 3C. As shown in the diagram, no cell death occurred in the PBS, NIR, or RCQD groups (Fig. 3C-a–c), indicating that these three groups had no ability to treat cancer cells. By contrast, the RCD + NIR and RCD–Pt(ɪᴠ)/PEG–CS–DA groups caused significant cell death (Fig. 3C-d and e), indicating that the two groups are beneficial for the cancer cell treatment based on PTT or chemo. Notably, almost all cells in the RCD–Pt(ɪᴠ)/PEG–CS–DA + NIR group died (Fig. 3C-f), indicating that RCD–Pt(ɪᴠ)/PEG–CS–DA exhibited superior capability for chemo/PTT, implying that the RCD–Pt(ɪᴠ)/PEG–CS–DA probes have potential for broad application in the chemo/PTT of tumors.

To evaluate the capability of RCD–Pt(ɪᴠ)/PEG–CS–DA for tumor microenvironment-induced cancer imaging in tumor-

bearing mice, RCD–Pt(ɪᴠ)/PEG–CS–DA was administered via subcutaneous injection into the tumor site and via caudal vein injection. The flow and targeted release of RCD–Pt(ɪᴠ)/PEG–CS–DA in vivo was then tracked based on fluorescence imaging. The results are presented in Fig. 4A. When administered into the tumor site via subcutaneous injection, RCD–Pt(ɪᴠ)/PEG–CS–DA could complete Pt(ɪɪ) release in the tumor tissue after 30 min, the RCDs could enter the tumor tissue and remained stable for 10 h, maintaining its same degree of fluorescence intensity. After injecting RCD–Pt(ɪᴠ)/PEG–CS–DA for 48 h, the tumor tissue still exhibited strong fluorescence (Fig. 4A-a). These results indicate that RCD–Pt(ɪᴠ)/PEG–CS–DA injected subcutaneously into the tumor site did not flow to other parts of the mouse. Instead, they were collected simultaneously within the tumor tissue and were stably maintained for 10 h and then gradually metabolized. After 48 h, some of the RCDs and Pt(ɪɪ) remained in the tumor tissue, which was favorable for synergistic chemo/PTT. After administration via caudal vein injection for 4 h, RCD–Pt(ɪᴠ)/PEG–CS–DA was mostly delivered to the tumor site. The acidic environment of the tumor cells allowed rapid PEG–CS–DA hydrolysis and RCD–Pt(ɪᴠ) release. High GSH levels in cancer cells reduced Pt(ɪᴠ) to Pt(ɪɪ) and released the RCDs, which then resulted in cancer tissue imaging. The fluorescence intensity remained unchanged within 4–10 h. After 48 h, the tumor tissue still showed strong fluorescence (Fig. S4, ESI†). These results indicate that RCD–Pt(ɪᴠ)/PEG–CS–DA exhibits excellent capability for tumor imaging, and targeted transport and release of Pt(ɪɪ).

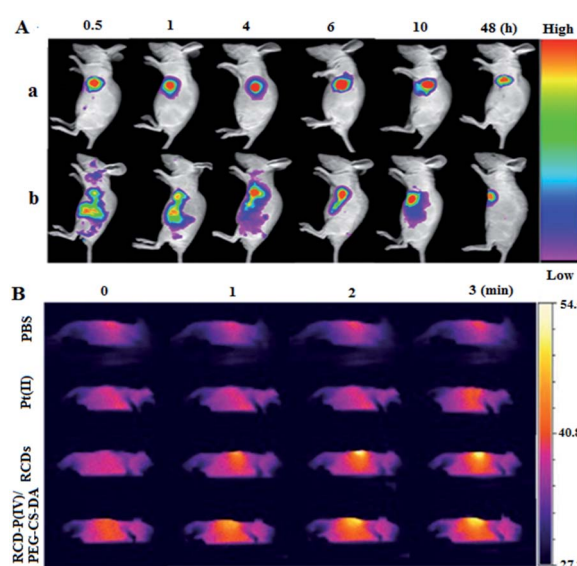The photothermal effects of PBS, Pt(ɪɪ), RCDs, and RCD–Pt(ɪᴠ)/PEG–CS–DA on tumor sites in tumor-bearing mice were

Fig. 4 (A) Tumor microenvironment-induced cancer imaging of tumor sites in vivo in tumor-bearing mice. Excitation wavelength: 630 nm; emission wavelength: 680 nm. (a) Subcutaneous injection of RCQD-Pt(ɪᴠ)/PEG–CS–D; (b) intravenous injection of RCQD–Pt(ɪᴠ)/PEG–CS–D. (B) Thermal imaging of tumor sites in vivo in tumor-bearing mice by using a 680 nm laser (1.5 W cm^{-2}) to illuminate the tumor site in vivo.

also investigated by thermal imaging. The tumor site *in vivo* was irradiated with a 680 nm laser (1.5 W cm^{-2}). Thermal imaging of tumor sites in mice was then performed at different time points, and the results are shown in Fig. 4B. As can be seen in the diagram, the temperature of the tumor sites in the PBS and Pt(II) groups almost remain unchanged during laser irradiation for 3 min, whereas that at the tumor site in the RCD and RCD–Pt(IV)/PEG–CS–DA groups increased to about 52 °C (Fig. S5, ESI†). These results suggest that the increase in temperature at the tumor sites in mice is attributed to neither PBS nor Pt(II) but to the photothermal effects of RCDs and RCD–Pt(IV)/PEG–CS–DA *in vivo*; moreover, the capabilities of both for photothermal conversion are similar, which proves that RCDs and RCD–Pt(IV)/PEG–CS–DA can be used as PTT photothermal reagents for the treatment of tumors.

In order to evaluate the efficacy of synergistic tumor therapy using RCD–Pt(IV)/PEG–CS–DA as a therapeutic agent, the tumor-bearing mice were treated for 14 d under different conditions. First, the tumor-bearing mice were divided into four experimental groups. Then, the PBS, Pt(II), RCD, and RCD–Pt(IV)/PEG–CS–DA solutions were injected, respectively, into the tumor-bearing mice *via* caudal vein injection. After the injection of therapeutic agents for 10 h, each group underwent respective laser irradiation and no laser irradiation. The experimental results for each group are presented in Fig. 5. The therapeutic effects largely varied under different conditions. During treatment, rapid tumor growth was observed in the PBS and PBS + NIR laser irradiation groups, whereas slightly inhibited tumor growth was found in the RCD, Pt(II), and Pt(II) + NIR laser irradiation groups. By contrast, significantly inhibited tumor growth was observed in the RCD–Pt(IV)/PEG–CS–DA group (chemo alone). The reason is that RCQD–Pt(IV)/PEG–CS–DA is stable in a normal physiological environment, and can achieve

targeted drug transport by enhanced permeability and the retention effect. Therefore, the RCD–Pt(IV)/PEG–CS–DA group exerts a good chemo effect, but still fails to completely inhibit tumor growth. Meanwhile, the therapeutic effect of the tumor-bearing mice in the RCDs + NIR laser irradiation group (PTT alone) was similar to that in the chemotherapy group alone. However, the tumor growth still could not be completely inhibited. Notably, in the RCD–Pt(IV)/PEG–CS–DA + NIR laser irradiation group (chemo and photothermal synergistic treatment), the tumor almost completely disappeared after treatment for 7 d, and no tumor regrowth was observed in the subsequent treatment (Fig. 5B).

After treatment for 14 d, the mice were dissected, and the tumor tissue was removed. A photograph of the tumor tissue is presented in Fig. 5C. These results suggest that neither chemotherapy alone nor PTT alone can completely eliminate tumor cells, and both can cause tumor recurrence. RCD–Pt(IV)/PEG–CS–DA as a therapeutic agent exerts an ideal therapeutic effect by using chemical and photothermal synergistic therapy.

To assess the pathological changes in the tumor tissue after chemo/PTT synergistic treatment for 1 week, the tumor tissue was subjected to hematoxylin–eosin (H&E) staining for histological analysis, and the pathology was observed by using an optical microscope. As can be seen in Fig. 5D, the tumor cells in the RCDs + NIR and RCD–Pt(IV)/PEG–CS–DA ± NIR groups exhibit obvious nuclear shrinkage, indicating apoptosis and necrosis of tumor cells. By contrast, the tumor cells in the RCD, PBS, Pt(II), PBS + NIR and Pt(II) + NIR groups remain closely arranged, indicating no significant damage. Therefore, from a pathological perspective, RCD–Pt(IV)/PEG–CS–DA as a therapeutic agent in the chemo and photothermal synergistic therapy exerts an ideal therapeutic effect.

To evaluate the toxicity and side effects of the treatment system on the main organs in mice, the tumor-bearing mice were divided into 3 groups, which were treated with PBS, RCD–Pt(IV)/PEG–CS–DA + NIR, and Pt(II). After treatment for 14 days, the mice were dissected and the main organs of the body, including the heart, liver, spleen, lungs, and kidneys, were removed. The organs were then sliced into sections and H&E-stained for histological analysis. The results are presented in Fig. 6. No significant damage was observed in the main organs
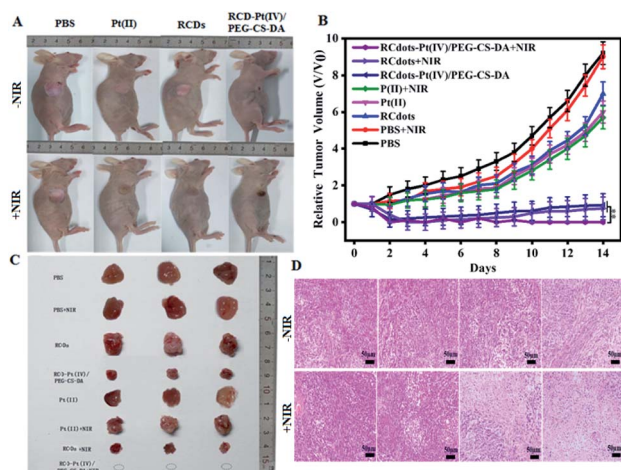

Fig. 5 (A) Representative photographs of mice from the 8 groups with different treatments after 14 days. (B) Tumor volume *versus* treatment time. (C) Photograph of dissected tumors after 14 days. (D) H&E-stained tumor tissues of mice from the 8 groups with different treatments after 14 days. The error bar represents the standard deviation (n = 3). The statistical analysis was performed using the Student's t-test method, **$p < 0.01$.
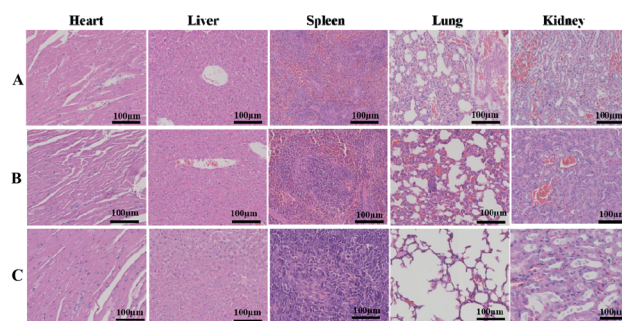

Fig. 6 H&E-stained tissues of the heart, liver, spleen, lung, and kidney of mice from the PBS (A), RCD–Pt(IV)/PEG–CS–DA + laser irradiation (B) and Pt(II) (C) groups after treatment for 14 days.

of the PBS and RCD–Pt(IV)/PEG–CS–DA + NIR groups (Fig. 6A and B). Nonetheless, damage at varying degrees was observed in various organs of the mice in the Pt(II) group (Fig. 6C). As shown in Fig. S6 (ESI†), during treatment, the body weights of the mice in the Pt(II) and Pt(II) + NIR groups decrease significantly, whereas those in the RCD–Pt(IV)/PEG–CS–DA + NIR group do not change significantly, indicating that the mice in the RCD–Pt(IV)/PEG–CS–DA + NIR group have considerably less toxic side effects than those in the Pt(II) and Pt(II) + NIR groups. These results further demonstrate that RCD–Pt(IV)/PEG–CS–DA as a synergistic chemo/PTT agent has obvious targeting ability. It not only shows a remarkable therapeutic effect but also has few side effects and significant potential for application in tumor therapy.

Conclusions

In summary, we prepared CDs with NIR absorption and emission, referred to in this study as RCDs, with natural biomass (*Osmanthus* seed peel) as the raw material, by using the solvothermal method. The RCDs obtained from natural biomass are easily surface-functionalized and exhibit good biocompatibility, low toxicity, high photothermal conversion efficiency, and NIR fluorescence emission. On the basis of the characteristics of the RCDs, we designed and constructed a multifunctional nanoprobe (RCD–Pt(IV)/PEG–CS–DA) for tumor microenvironment-induced cancer imaging and chemo/PTT synergistic targeted therapy. The *in vivo* study results suggest that the developed nanoprobes have several significant advantages. First, tumor microenvironment-induced cancer tissue imaging can image solid tumors in real time to obtain an accurate diagnosis of cancer diseases. Second, tumor microenvironment induced targeted release of Pt(II) drugs can overcome cisplatin resistance, prevent side effects on normal cells, improve the safety of normal tissues, and provide new ideas for the development of platinum drug transport systems. Third, synergistic chemotherapy and PTT can considerably improve the efficacy of tumor treatment. Therefore, the proposed strategy has great application prospects in the diagnosis and efficient treatment of clinical tumors.

Conflicts of interest

There are no conflicts to declare.

Acknowledgements

Notes and references

1 K. Heinzmann, L. M. Carter, J. S. Lewis and E. O. Aboagye, *Nat. Biomed. Eng.*, 2017, **1**, 697–713.
2 M. Gao, F. Yu, C. Lv, J. Choo and L. Chen, *Chem. Soc. Rev.*, 2017, **46**, 2237–2271.
3 V. MacDonald, *Can. Vet. J.*, 2009, **50**, 665–668.
4 D. J. Burgess, *Nat. Rev. Cancer*, 2012, **12**, 377.
5 H. Y. Yang, M. S. Jang, Y. Li, Y. Fu, T. P. Wu, J. H. Lee and D. S. Lee, *J. Controlled Release*, 2019, **301**, 157–165.
6 Y. Liu, P. Bhattarai, Z. Dai and X. Chen, *Chem. Soc. Rev.*, 2019, **48**, 2053–2108.
7 C. Wang, H. Tao, L. Cheng and Z. Liu, *Biomaterials*, 2011, **32**, 6145–6154.
8 R. Xing, Q. Zou, C. Yuan, L. Zhao, R. Chang and X. Yan, *Adv. Mater.*, 2019, **31**, 1900822.
9 Z. Wang, X. Zhen, P. K. Upputuri, Y. Jiang, J. Lau, M. Pramanik, K. Pu and B. Xing, *ACS Nano*, 2019, **13**, 5816–5825.
10 A. Zhang, A. Li, W. Zhao and J. Liu, *Chem.–Eur. J.*, 2018, **24**, 4215–4227.
11 P. Tang, Y. Liu, Y. Liu, H. Meng, Z. Liu, K. Li and D. Wu, *Biomaterials*, 2019, **188**, 12–23.
12 J. Du, Z. Gu, L. Yan, Y. Yong, X. Yi, X. Zhang, J. Liu, R. Wu, C. Ge, C. Chen and Y. Zhao, *Adv. Mater.*, 2017, **29**, 1701268.
13 S. Sun, J. Chen, K. Jiang, Z. Tang, Y. Wang, Z. Li, C. Liu, A. Wu and H. Lin, *ACS Appl. Mater. Interfaces*, 2019, **11**, 5791–5803.
14 F. Yin, K. Hu, Y. Chen, M. Yu, D. Wang, Q. Wang, K. Yong, F. Lu, Y. Liang and Z. Li, *Theranostics*, 2017, **7**, 1133–1148.
15 Y. Tao, E. Ju, J. Ren and X. Qu, *Biomaterials*, 2014, **35**, 9963–9971.
16 H. Ye, K. Wang, M. Wang, R. Liu, H. Song, N. Li and J. Sun, *Biomaterials*, 2019, **206**, 1–12.
17 L. Kelland, *Nat. Rev. Cancer*, 2007, **7**, 573–584.
18 T. Langer, A. A. Zehnhoffdinnesen, S. Radtke, J. Meitert and O. Zolk, *Trends Pharmacol. Sci.*, 2013, **34**, 458–469.
19 Z. Cheng, Y. Dai, X. Kang, C. Li, S. Huang, H. Lian and J. Lin, *Biomaterials*, 2014, **35**, 6359–6369.
20 Y. Min, J. Li, F. Liu, E. K. Yeow and B. Xing, *Angew. Chem., Int. Ed.*, 2014, **126**, 1030–1034.
21 H. Xiao, H. Song, Q. Yang, H. Cai, R. Qi, L. Yan, S. Liu, Y. Zheng and X. Jing, *Biomaterials*, 2012, **33**, 6507–6519.
22 H. Xiao, H. Song, Y. Zhang, R. Qi, R. Wang, Z. Xie, Y. Huang, Y. Li, Y. Wu and X. Jing, *Biomaterials*, 2012, **33**, 8657–8669.
23 Y. Li, G. Bai, S. Zeng and J. Hao, *ACS Appl. Mater. Interfaces*, 2019, **11**, 4737–4744.
24 W. Yang, B. Wei, Z. Yang and L. Sheng, *J. Inorg. Biochem.*, 2019, **193**, 166–172.
25 B. Ryplida, G. Lee, I. In and S. Y. Park, *Biomater. Sci.*, 2019, **7**, 2600–2610.
26 T. Feng, X. Ai, G. An, P. Yang and Y. Zhao, *ACS Nano*, 2016, **10**, 4410–4420.
27 Y. H. Bae and K. Park, *J. Controlled Release*, 2011, **153**, 198–205.
28 H. Maeda, J. Wu, T. Sawa, Y. Matsumura and K. Hori, *J. Controlled Release*, 2000, **65**, 271–284.
29 T. S. Hauck, T. L. Jennings and T. Yatsenko, *Adv. Mater.*, 2008, **20**, 3832–3838.
30 T. B. Huff, L. Tong, Y. Zhao, M. N. Hansen, J. X. Cheng and A. Wei, *Nanomedicine*, 2007, **2**, 125–132.